THESIS FOR THE DEGREE OF LICENTIATE OF ENGINEERING IN
MATERIALS SCIENCE

Modelling and Experimental Design of a High Resolution X-ray Detector

LARS HAMMAR

Department of Materials and Manufacturing Technology

CHALMERS UNIVERSITY OF TECHNOLOGY

Gothenburg, Sweden 2013

Modelling and Experimental Design of a High Resolution X-ray Detector
LARS HAMMAR

"In the kingdom of the blind, the one eyed man is king"

-Desiderius Erasmus (1466-1536)

Modelling and Experimental Design of a High Resolution X-ray Detector
Thesis for degree of Licentiate of Engineering in Materials Science
LARS HAMMAR
Department of Materials and Manufacturing Technology
Chalmers University of Technology

Abstract

In aging power plants the number of service induced defects tends to increase over time. Beside fatigue and corrosion problems the nuclear power plant sometimes has problems with flaws due to stress corrosion cracking (SCC). A non-destructive testing method such as ultrasonic technique (UT) is normally used to in order to detect and monitor such crack growth. There are several materials with inappropriate microstructure that are not suitable for ultrasonic inspection and in these cases radiographic testing (RT) could be a better alternative. A radiographic system, that has sufficient radiographic sensitivity in order to detect and to characterize SCC, has been developed. The objective has been to achieve highest possible image quality by detecting as many primary photons as possible with minimal possible pixel size.

One of the objective of this work has been, on the basis of Monte- Carlo simulations of detection process, identify that the deposition of energy in the scintillation screen is very local. By using glass fiber optic technology the high spatial resolution has been preserved through the optical chain into the CCD-sensor. Monte-Carlo simulations are used to show how to minimize the radiation induced noise in the detector. Noise, origin from the x-ray source, but also from the radioactive environment.

Verifying tests with the new detector have been evaluated. The radiation induced noise has been decreased to a level less than 1% compared with the previous construction. The conclusion is that the radiographic sensitivity is further improved and fare beyond what is achievable with fine grained radiographic film.

Keywords: Digital Radiography, Nuclear Power, X-ray, Detector, Scintillation, Fiber Optics, Crack Detection, Non Destructive Testing

Preface

Thesis

The thesis consists of two parts: a summary of the performed work and appended papers resulting from the work. The papers are:

Paper I
Development of a High Resolution X-ray Radiographic Technique, Optimized for On-site Testing in Radioactive Environments,
Hammar L., Wirdelius H., 16th World Conference on Nondestructive Testing, Montreal 2004

Paper II
Modelling of High Resolution Radiographic System and Development of a Filtering Technique Based on Wavelet Transformation,
Wirdelius H., Hammar L., NDT&E International vol. 37, p.73, 2004

Paper III
Radiographic Sensitivity Improved by Optimized High Resolution X-ray Detector Design,
Hammar L., Wirdelius H., Int. Symposium on Digital Industrial Radiology and Computed Tomography, Lyon, 2007

Paper IV
Novell design of high resolution imaging x-ray detectors,
Hammar L., 18th World Conference on Nondestructive Testing, Durban 2012

Contents

1 Introduction

1.1 Cracks

Cracks and other imperfections are always present in all kind of manufactured materials and the main question is when these are defined as defects. The most general definition is the one that specifies a correlation to a significant impact on the components integrity. Normally cracks are defined as macro cracks if their length is in the magnitude of a few tenths of a millimeter and up. Cracks are also divided in internal and surface breaking cracks as well as dependent on origin from the manufacturing process (e.g. welding) or if they are service induced.

Stress corrosion cracking (SCC) is a severe degradation mechanism addressed in many in-service inspection programs in nuclear power plants. The propagation of these kinds of cracks is due to a combination of material composition, tensile stress and environmental conditions. There are two major types that will be analysed here, intergranular stress corrosion cracking (IGSCC) and interdendritic stress corrosion cracking (IDSCC). There is also a third mechanism, transgranular stress corrosion cracking (TGSCC), but it needs a chloride concentration to propagate which never occur under normal conditions.

There are three major factors that cause IGSCC to form and propagate (along the grain boundaries). These are tensile stresses on the inner diameter of the weld region, a corrosive environment and a sensitized grain structure[1]. Nuclear power plants of the boiling water reactor type with welds in austenitic stainless steel fulfil these conditions. The cracks are often found in the heat affected zone (HAZ) which is base material adjacent to the weld. The detection of IGSCC in the HAZ of welds in austenitic stainless piping is therefore of considerable interest to the nuclear industry.

Inter dendritic stress corrosion cracking (IDSCC) is usually found in the centre of the weld in nickel based alloys and not in the heat affected zone as IGSCC. The expected surface direction of IDSCC follow the weld while IGSCC is usually parallel to the weld, otherwise IDSCC is similar to IGSCC. They always start from the inner surface due to the corrosive environment and weld stresses.
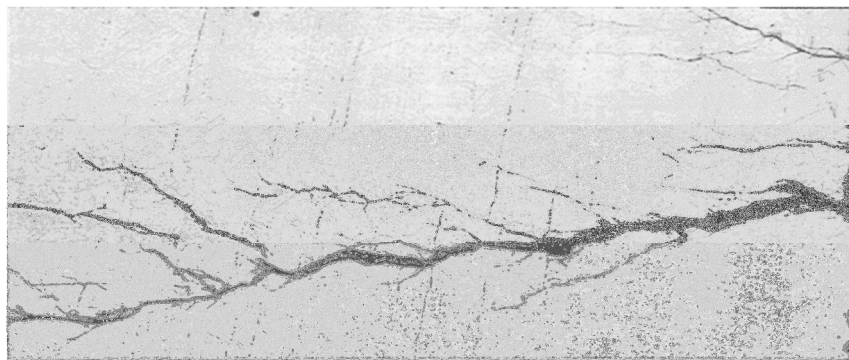
Figure 1. Typical IGSCC with branches.

The cracks spread in the depth direction in the grain boundaries and they wind down under the surface. The variation in sideway direction is called surface roughness of the crack and is

defined in the same way as common surface roughness. This surface roughness[2] is in same magnitude as the grain size of the current material. The crack opening width (which is the same as crack opening displacement, COD) for a five mm deep IGSCC is typically 25-50 µm. Since radiographic technique is based on projections of volumetric information (3-dim) into a 2-dimensional array with variations, in gray scale, this small scale variation is blurred out in a single x-ray image.

1.2 Crack detection

It does not exist anyone non-destructive testing method, that can pretend to be universal. Most methods are specific for certain types of defects and materials. It is important that the selected method can give information with respect to its sensitivity for the types of defects that one is looking for. Knowledge about the materials composition, homogeneity and structure are important as well as the expected position and orientation.

If the crack is surface breaking or close to the surface a non-destructive method like magnetic particle (MT), penetrant testing (PT) or eddy-current (ET) are chosen[3]. They are all surface sensitive methods but they give little or no information from the depth.

Ultrasonic testing using an angle beam is the standard non-destructive testing method for in-service inspection of SCC. This method involves launching an ultrasonic wave into the weld region, and analyzing the signal reflected back from a discontinuity present within the material. This works excellent in ferritic steels but it is much more difficult in austenitic stainless steels. The attenuation of the ultrasound is high, particularly at high frequencies. The anisotropic grain structure causes the ultrasonic beam to bend. In the case of IDSCC is the situation even worse because the cracks are in the weld metal where the microstructure makes ultrasonic testing inappropriate.

As mentioned earlier, x-ray radiography is a volumetric NDT-method and consequently not the first choice for crack detection. Fatigue cracks e.g. can be closed in the absence of stress and consequently there is very little volume inside the crack. In the case with IGSCC or IDSCC there is always a certain COD due to the welding stresses. It can be showed with fracture mechanics[4] that the volume is somewhat proportional to the COD and also to the depth of the crack.

$$U(x) = \frac{2(1-v^2)}{E}\sigma_\infty\sqrt{a^2 - x^2} \tag{1}$$

Where $U(x)$ is the COD, σ_∞ is the welding stress[1] and a the depth of the crack.
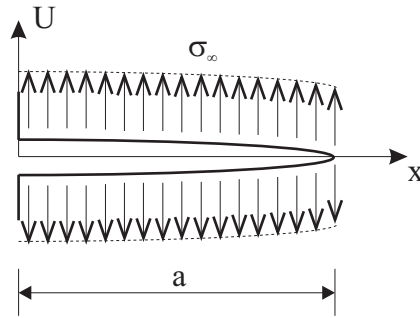
Figure 2. Weld stresses.

By using the relation between width and depth of the crack it can be expressed as the volume of the crack. A line profile across the difference in contrast, as the projected volume from the crack gives origins to, contains valuable information. The line profile integral is proportional to the volume of the crack and can be translated to radiographic contrast.

If the resolution and image quality is sufficiently high and the procedure incorporates adequate numbers of exposures within an angle interval, the system has the capacity of detecting, sizing and characterizing IGSCC over a certain size[3].

A High Resolution X-ray system (HiReX) (see Figure 3) was developed 1997 for characterizing service induced intergranular stress corrosion cracking (IGSCC) in nuclear power plants[5]. The aim with the system was to reach as high radiographic sensitivity as possible at the same time as the physical size of the detector is minimized.
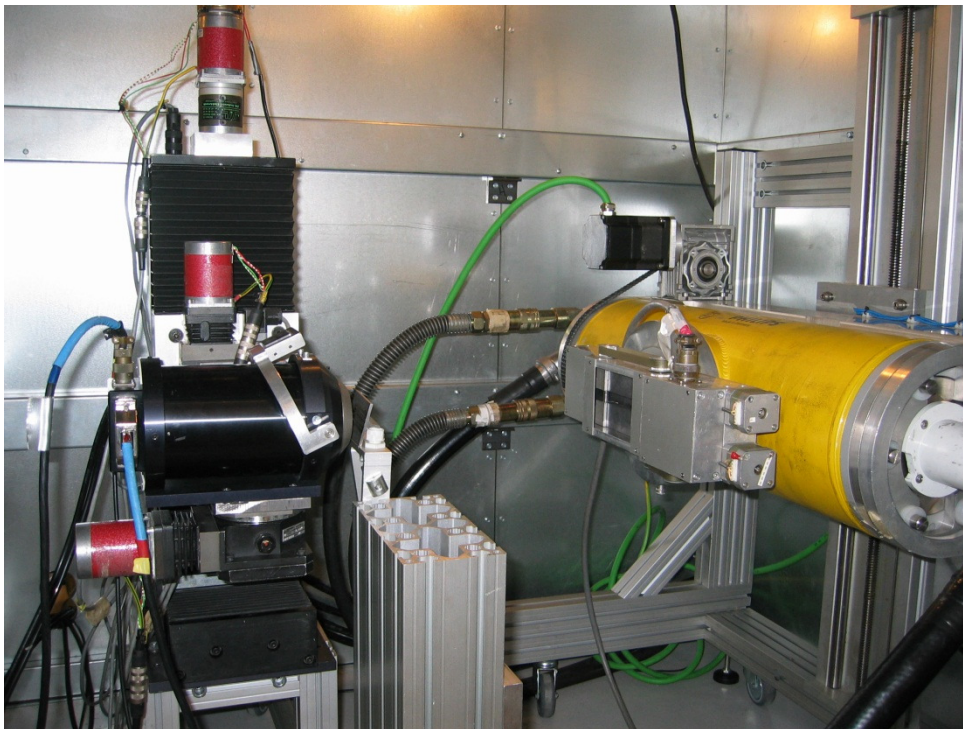
Figure 3. HiReX system

The system is based on scintillating fiber optical faceplates (SFOP) along with a fiber optic lens and a cooled CCD element. The system reaches higher spatial resolution than fine grained X-ray film concurrent as detection efficiency is increased. The light guiding structure of an optical fiber allows the thickness of the scintillating faceplate to be increased to 10 mm with only a moderate degradation of the spatial resolution.

Earlier studies[6] have shown that energy deposition from an x-ray photon is very local and by simulating [7] an impulse response, it is possible to determine what spatial resolution that is theoretically achievable. The difference between the theoretical and the achieved resolution depends, according to a study[8], on the internal light spread.

Another design issue with HiReX was the fiber optic lens that wasn't sufficiently long in order to protect the CCD element against primary radiation. Modern CCD chip has extremely good performance but is also very sensitive for damages caused by ionizing radiation. Thus it has to be protected by an appreciably longer fiber optic lens or it has to be moved out from the primary beam. Mathematical modeling of the system using Monte Carlo simulation has been used in order to solve this design issue[9].

2 X-ray technique

2.1 X-ray imaging

When x-rays have pass an object it contains spatial variations in intensity that is caused by defects, discontinuities or variation in density and attenuation (atomic number). If there are defects in an object these will create variations (contrast) in the intensity of the detected x-rays. The defects or in-homogeneities are finally viewed as variations of gray scale in an x-ray image. As the attenuation process arises in the object it is more or less independent of the detecting medium. The detecting medium or the detector converts the variation in attenuation to a gray scale image [3].
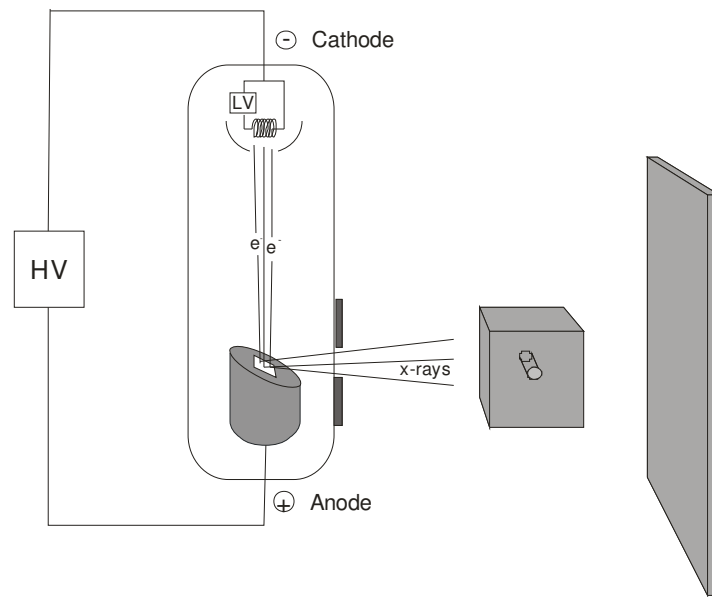

**Figure 4. Principles of x-ray radiography.**

2.2 Optimization of image quality

There are two main parameters that govern the image quality and the radiographic sensitivity that can be achieved. The first is unsharpness and the second is the detection efficiency or the number of detected primary x-ray photons. As x-ray radiography is here defined as a static process, there is no motion unsharpness.

The first factor is the total unsharpness[3] (U_t) which is the combination of geometric unsharpness (U_g) and the detector unsharpness (U_f). U_g is caused by the focus size in the x-ray tube and the relation between the position of the object and the detector. The U_f is a way to define the spatial resolution of the detector. The U_f is defined as the first unresolved wire pair measured with a double wire[9] image quality indicator (IQI) according to the SS-EN462-5[10] standard. The unsharpness is the same as the first wire where modulation is less than 20%. The basic spatial reolution (SR_b) is defined as:

$$SR_b = \frac{U_f}{2} \tag{2}$$

This is not same as the pixel pitch (or pixel size) but rather considered as the effective pixel pitch.
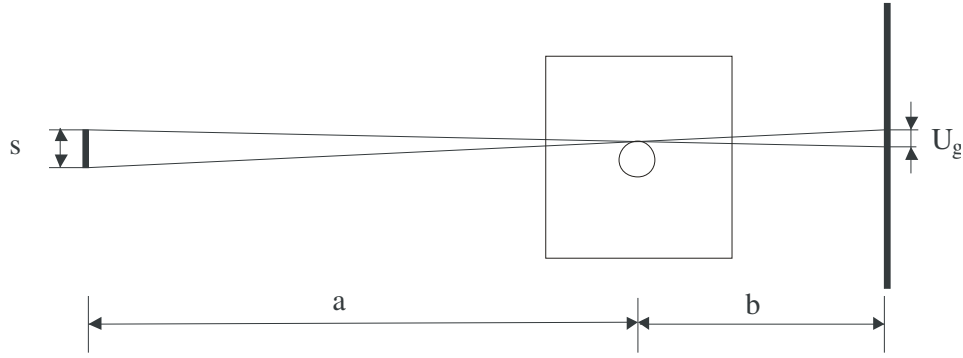
Figure 5. Unsharpness.

$$U_g = s \cdot b / a \qquad\qquad\qquad (3)$$

$$U_t = \sqrt{U_g{}^2 + U_f{}^2} \qquad\qquad\qquad (4)$$

A theoretically optimum X-ray system would comprise of an x-ray source with infinite effect and an infinitesimal focus size, together with a detector with infinite spatial resolution. Since the power per unit area at the focal point has a maximum, before the anode gets thermally damaged, the size of the focus can't be infinitesimal. There is so-called micro focus tubes[3] were electrostatic focusing of the electron beam results in a very small focus point (s E 1μm) but at the expense of power that leads to very low intensity in the primary beam. The total thickness can often be from 40 mm and up in the nuclear piping components addressed by in-service inspection. The reason that the thicker wall thicknesses are more interesting to inspect is that they usually are part of the main systems that are difficult to replace. Smaller dimensions are often used in help systems, and these are easier to replace which is the easiest way to get rid of the problem. In the thicker parts, it is possible to monitor the potential crack growth with an inspection program. That leads to the exclusion of micro focus tubes were the accelerating voltage isn't sufficiently high (up to 320 kV). The natural choice is so-called contact technique in which the detector is positioned close to the test volume as opposed to micro focus technique were the focus is positioned close to the same.

The x-ray tube focus size[11] is measured to 0,4 mm (deviation from EN12543-2 standard[12], evaluation of the focal spot based on 25% threshold) in the new system, optimized by the expected size of the test object. With a test object, e.g. typical nuclear pipe component with a diameter of 400 to 500 mm and a wall thickness of 30 mm. The parameters, a=600 mm and b= 50 mm. This gives a total unsharpness of 33 μm.

The number of detected primary photons (N) is the second main parameter. X-rays are statistical to its nature and follows the Poisson distribution which passes on to the normal distribution when the number of event is large. This means that the statistical noise or the standard deviation is equal to the square root of N[13]. This relationship is also called signal-to-noise ratio (SNR).

$$SNR \sim 1/\sqrt{N} \qquad\qquad\qquad\qquad\qquad (5)$$

The scattered radiation, in conventional radiography, contains no information and contributes only with noise. The amount of scattered radiation are defined as the "built-up"-factor[3] (BF) and is the quota between scattered (I_S) and direct radiation (I_D). See Eq. (6).

$$BF = 1 + \frac{I_S}{I_D} \qquad\qquad\qquad\qquad\qquad (6)$$

The use of a 1-dim array is the only way to avoid the problem completely, which then decreases the efficiency dramatically. When an object with a thickness of 50 mm steel is inspected with energy at 400 kV, the BF is approximately six. BF can be decreased either by using filter or increasing the object-detector distance
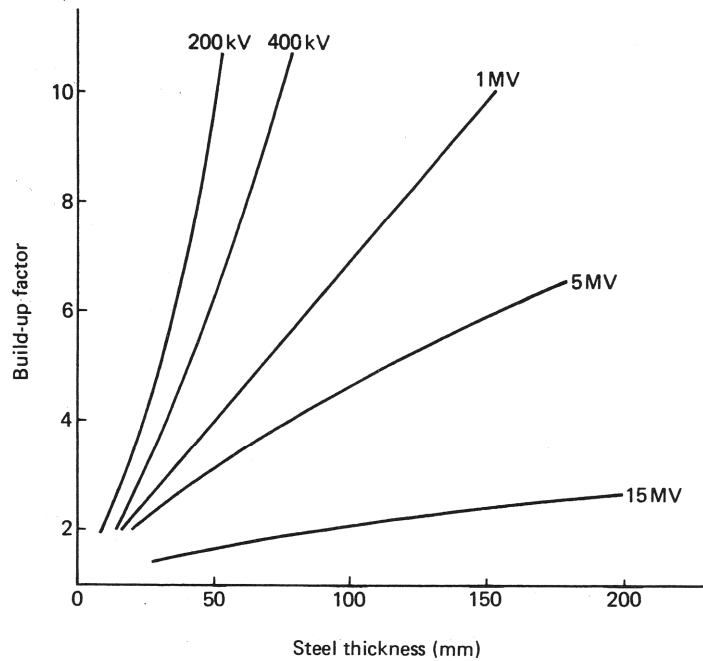

Figure 6. "Built-up" factor (BF).

2.3 X-rays and its interaction with matter

X-ray tubes are high voltage devices that convert electrical energy into x-rays. An x-ray tube consists of a cathode structure containing a filament and an anode structure containing a target, all within an evacuated chamber or tube. A low-voltage power supply generates the electric current that heats the filament to glow, which thermally liberates the electrons. They are then accelerated to the anode by the high voltage applied between the cathode and the anode. When the electrons hit the anode material, they are stopped and deflected as they interact with the electric field around the atoms, and the kinetic energy of the electrons is converted into x-ray energy. The produced x-ray energy is a continuous spectrum[14] and the characteristic x-ray peaks. See Figure 7.
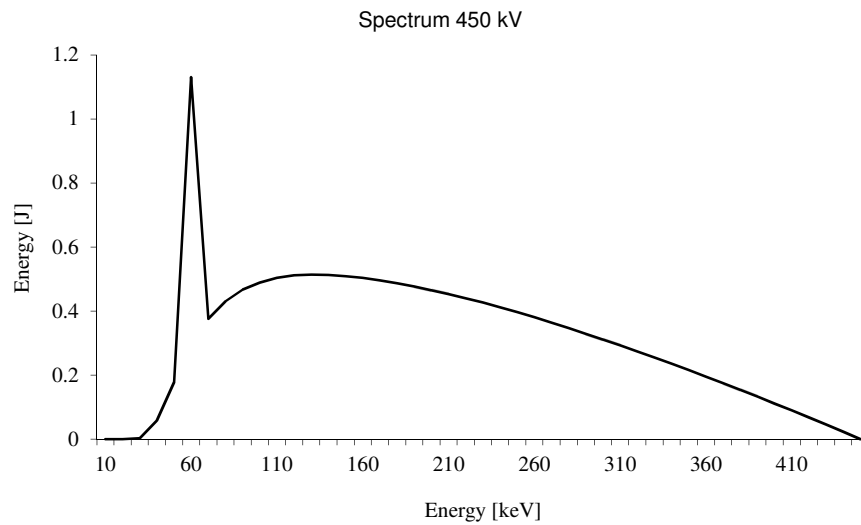
Figure 7. Spectrum from an 450 kV x-ray tube (tungsten anode).

X-ray photons interact with any matter as the rays pass through the object. For mono-energetic radiation the intensity varies exponentially with the thickness of the material as[15]:

$$I = I_0 \cdot e^{-\int_L \mu(x)dx} \qquad (7)$$

Where I is the intensity after the object, I_0 is the initial intensity, x is the thickness, and μ is the linear absorption coefficient[16].

An X-ray beam consists of photons of a given energy spectrum[14]. The photon as such has no charge or rest mass, which means that it can't be detected directly, but only indirectly. There are several ways for photons to interact with matter, but for radiography (E < 1,022 MeV) these can be divided into three possible processes. The radiation can knock out electrons from atoms and ionize them or the radiation can knock out electrons from the atoms so they will be excited. The radiation may also hit the atom which leads to "elastic" scattering. It is important to emphasize that it is not the particles themselves that collide, it is their electric fields.

The photons are attenuated (absorbed and spread) as they travel through the object to the detector. The processes that are relevant are[17]:

- Coherent (Rayleigh) scattering: Scattering of photons in small angles without any loss of energy.
- Incoherent (Compton) scattering: Scattering of photons with energy loss resulting in a Compton photon and a recoil-electron.
- Photo effect: An electron is knocked out with subsequent secondary effect, such as emission of characteristic X-ray.

3 Developments

3.1 Scintillation

The scintillation detector is one of the earliest detectors in radiology. It is an indirect detector which converts x-rays into visible light through the scintillation effect. It is the secondary emission of beta-particles from the primary detection process (photo- and Compton-effect) that excites the detector material. The absorbed beta-radiation interacts with the detector material and generates excitations and ionizations. It takes an average of 35 eV per interaction process to form an electron-hole pair[18]. Scintillation process in an inorganic crystal depends on its lattice structure. In a pure, inorganic crystal such as CsI, the electrons have certain allowed energy levels, where the absorbed energy can lift the electrons from the valence band to the conduction band. The problem is that the emission of a photon in this case is an inefficient process where also the width between the valence and conduction bands is so that the emitted photon is outside the visible wavelength range. See Figure 8. Small amounts of impurities added to the material to create sites (activation centres) in the structure, with a modified band gap. These sites are called luminescent or recombination centres.

Conduction band* — Activator exited state
X-ray photon —→
Valence band* — Activator ground state
*Pure crystal — Visible photon
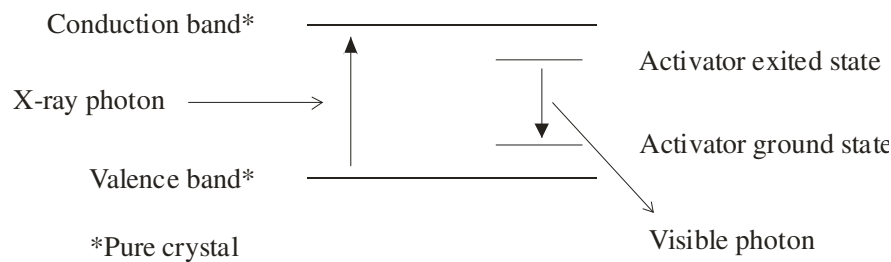
Figure 8. Energy band structure.

When a photon is attenuated by a doped crystal, a large number of electron-hole pairs are formed when electrons are excited into the conduction band. The positive holes drift towards activator centres and ionize them because the ionization energy is lower there. The electrons migrate freely in the crystal until they come to an ionized activator centre. Now, the electron can de-excite and the crystal emits light in the wavelength that is settled by the specific ion in the activator centre.

Some organic scintillators can be characterized by a single decay constant but often the decay sequence is more complex. Some electrons are excited to a level requiring additional energy for de-excitation. Then thermal excitation leads to a slow component of light called phosphorescence, which is the same as afterglow.

In the late 1940s it was discovered that NaI(Tl) (Sodium iodine doped with Thallium) was a scintillation material with exceptionally good properties. NaI is a crystalline material and with an additional doping of about 0.1 mol% Tl to create optimum amount of activator sites in the crystal lattice[19]. Its light peak is around 410 nm which matches to photo multiplication tube (PMT). The big advantage is its relatively high density and the high amount of light it yields.

Detectors based on scintillation works excellent at low energies (E50 keV) but the detection efficiency drops at higher energies. In order to increase the detection efficiency, the thickness

9

of the screen must be increased but at the expense of the spatial resolution. In conventional screens the scintillating material is in the form of powder and applied with adhesives. The light that is produced when x-ray are absorbed is emitted isotropically and only photons that have an angle less than E can be detected (See Figure 9). The rest is reflected back into the screen again. The spatial resolution is then proportional to the thickness of the screen.

2α
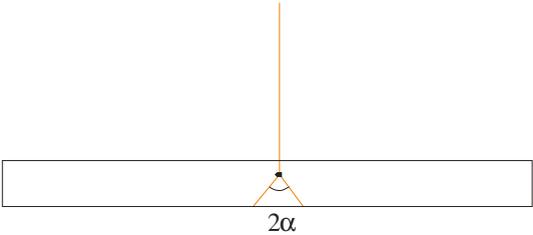
Figure 9. Light spread depends on the refraction indices.

One way to solve this problem is to guide the light through the scintillating screen. This can be done in several different ways but in practice it is two methods that are applicable. One way is to use structurally grown CsI(Tl)-crystals and another is to use scintillating glass fiber optic faceplates (SFOP)[20]. Screens made of structural grown CsI(Tl) is produced through chemical vapour deposition in a standard vacuum chamber. The crystals diameter can vary from 1 to approx 30 μm and the screens can be up to 3 mm thick. A real screen (10-40 μm) can reach a spatial resolution as high as 30 lp/mm (MTF =10%) but then detection efficiency is very low.
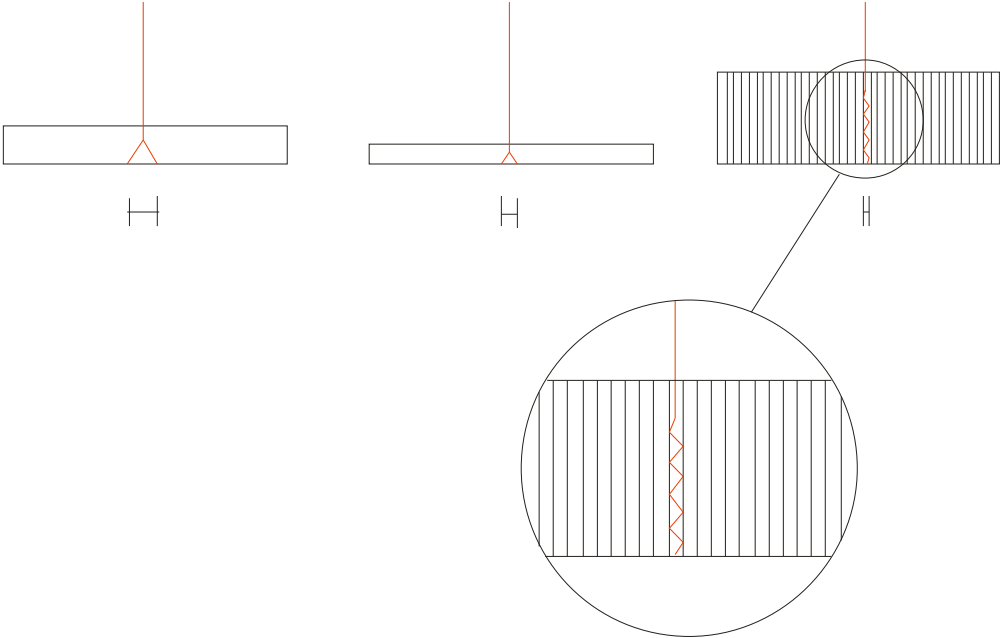
Figure 10. Light spread depends on thickness and light guiding.

When the thickness of the screen is increased, the diameter of the crystal also increases. A screen 1,5 mm thick is the diameter of the crystals measured to 32 μm[21]. The detection efficiency is appreciably higher but the resolution is only 2 lp/mm (MTF 10%). Since the crystals are not entirely perfect, the light guiding capability will not be perfect either. The light

spreading problem increases with increased thickness of the screen due to the fact that crystals, tends to become less perfect the longer the crystals are grown.

To study how the primary photons are attenuated, we will look at how much and at what depth the energy is deposited[22]. There are two types of scintillator material being compared, one with a 300 µm CsI (Tl)[20] and a scintillating SFOP (LHK-6)[23] with a thickness of 10 mm. For simplicity, the thickness of the scintillators is normalized to one. The next three figures show the attenuation as function of depth for each tenth of the thickness. In Figure 11 we can see that the detection efficiency is very good for CsI(Tl) but a little too high for LHK-6. Most of the deposited energy is attenuated in the first 20% of the thickness. When the energy is increased to 100 keV (see Figure 12) total detection efficiency is over 20% for CsI (Tl) while LHK-6 has almost 90%. In Figure 13 where the energy is increased to 300 keV the detection efficiency for CsI (Tl) is only 1.4% while it is 10% for LHK-6. It can also be seen that the distribution of the attenuated energy is much smoother at 300 keV. The first tenth attenuates only marginally more than the last.
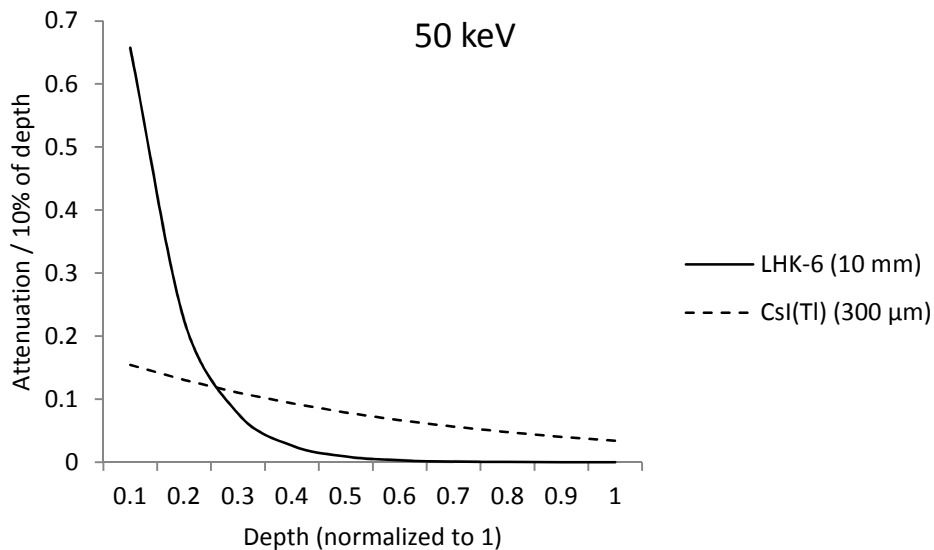
Figure 11. Attenuation depth 50 keV.
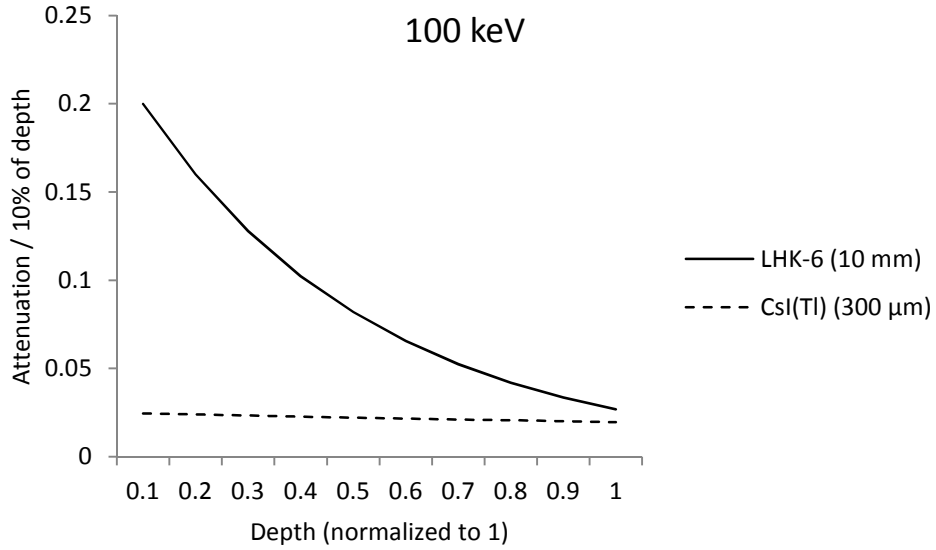
Figure 12. Attenuation depth 100 keV.
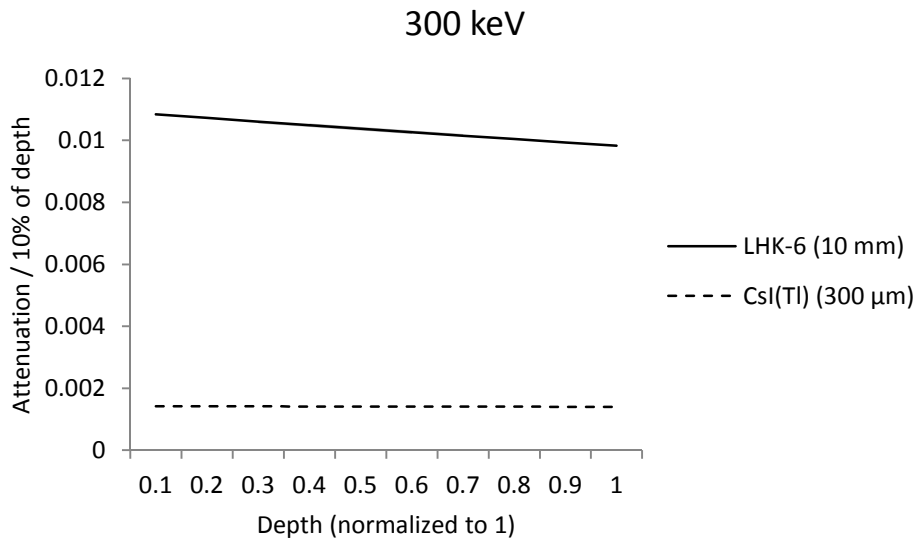
Figure 13. Attenuation depth 300 keV.

As previously mentioned SNR proportional to the square root of N, but it applies only to detection efficiency of 100%. A more accurate way to express SNR is as follows[24]:

$$SNR \sim \sqrt{N \cdot \eta} \tag{8}$$

As we see in Table 1, the detection efficiency at higher energies is relatively low for CsI (Tl) which is as expected as thickness is only 300 μm. By looking at the ratio between the respective detection efficiencies it can be seen that at 300 keV is more than 7 times as large. This shows the great advantage of using thick scintillating screen.

Energy [keV]	D_{eff} CsI(Tl) (300μm)	D_{eff} LHK-6 (10mm)	D_{eff} LHK-6/D_{eff} CsI(Tl)
50	0.81	1.00	1.23
100	0.21	0.89	4.25
300	0.014	0.10	7.33

Table 1. Detection efficiency of CsI(Tl) and LHK-6.

3.2 Monte-Carlo simulation of x-ray detection

The objective with the first Monte Carlo simulations was to estimate the energy deposition as function of the radial distance from the central axis in the SFOP screen. Also to estimate the radiation induced noise in the CCD.

A software package from Nuclear Energy Agency (NEA), Penelope[7], was used for the simulations. The Penelope software package is written in Fortran code and performs simulation of coupled electron/positron-photon transport in arbitrary materials. The adopted scattering model allows simulations in the range from 100 eV to 1 GeV, which covers the range of interest for detailed simulations of high energy industrial radiography. Penelope generates random electron-photon showers in complex structures consisting of distinct homogeneous bodies of different compositions. Penelope reads the required information about each material from a material data file. In the simulations of the fibre optic scintillation faceplate, the chemical composition of the scintillating glass is used as input and the output are tables of physical properties and interaction cross sections. The bodies are made out of homogeneous regions limited by quadric surfaces.

The bodies that can be simulated are planes, cylinders, spheres, paraboloids, etc. There are no limits in size and the simulations can thus be made on micron-sized objects as well as large objects. The simulations are very fast by using the reduced form of quadric surfaces.

The simulations are done to find the minimum useful pixel size. There are no concerns about optics in these simulations and it is assumed that the scintillating events during the absorption process produce light photons instantly.

3.3 Energy deposition

Earlier studies[6] have shown that the energy deposition is very local and which indicates a possibility to achieve higher resolution than with today's technology. An infinitesimal x-ray that is parallel to the normal axis to the detection surface is simulated. The beam goes from the focal spot, through a 50 mm high cylindrical test object (steel) and hits the detection surface in the centre of the scintillating faceplate (SFOP). Compton scattered radiation generated in the test object is excluded by using a filtered x-ray spectrum[25] corresponding to 50 mm of steel, with maximum energy of 450 keV. The detecting part of the x-ray camera is simulated as cylinders[25] with an aluminium front, SFOP and the frontal end of the fibre optic lens. Each individual photon is simulated where all relevant attenuation processes for x-ray photons and secondary beta particles are taken into account. The simulation of photons and secondary electrons is not aborted until the energy is less than 5 keV. This is sufficient as the so called continuous slowing down approximation range (CSDA) is approximately 0,1 μm for a 5 keV

electron[26]. The number of simulated primary photons were 140 000 which took 30 minutes on an ordinary portable PC (1,8 GHz processor). The detection surface is divided up in a square grid with 401x401 elements where the element side is 2 μm. The height on the elements is same as the scintillating faceplate, which is 10 mm. The result of the simulation is shown in Figure 14. The impulse response shows that the energy deposition is very local, then the amplitude falls dramatically and is < 0,1 on a distance of 10 μm from the centre. The effect of the scattered radiation is clearly visible in Figure 14 where the deposition of energy decreases with the radial distance from the center.
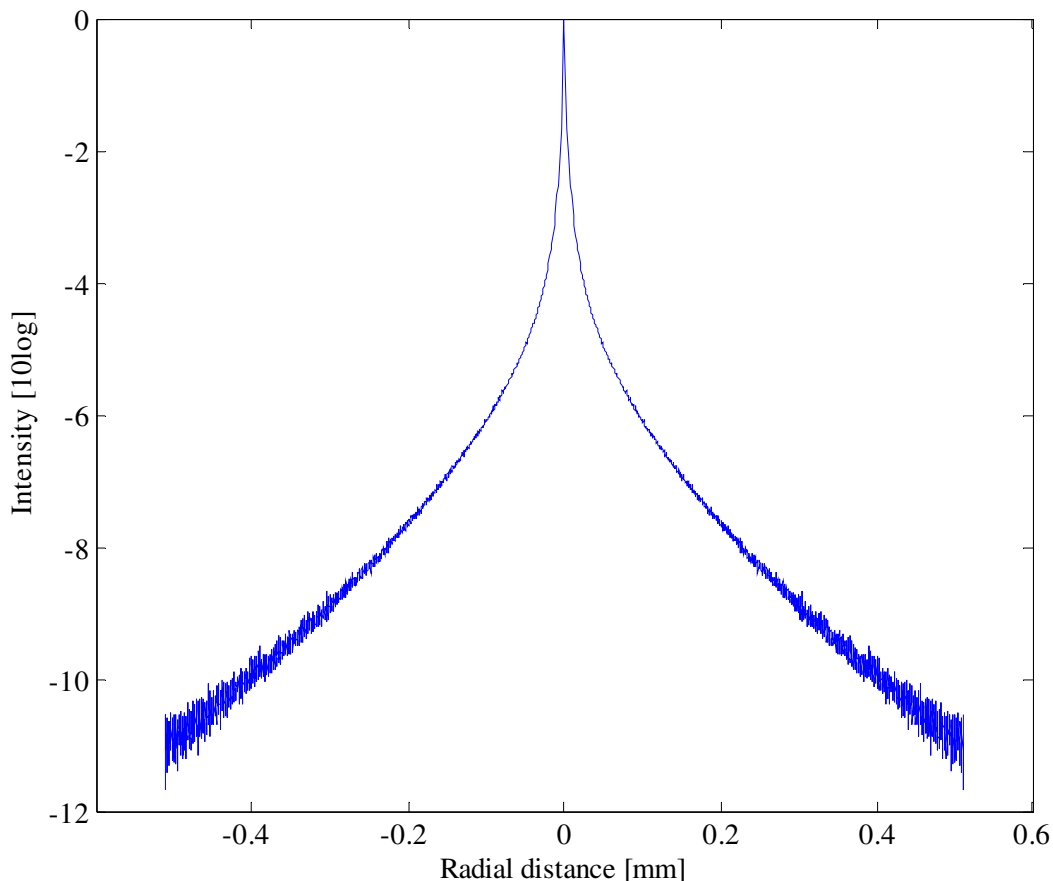
Figure 14. Radiological impulse response.

3.4 Fiber optics

A fiber optic light guide is a conductor of light and can be very flexible. It consists of a core with higher refraction indices and a cladding with a lower. The diameter varies from a few μm up to some millimeter. They can be produced in different types of glasses and polymers assumed that they have good light conducting properties and high transmission for the actual wavelengths. A glass fiber optic image conduit[27] is a solid unit of glass fibers which is sintered together.

An image conduit is used to transport light and is considered as a perfect lens, without aberrations. It can also be used as an x-ray detector if the core glass has scintillating properties.

14
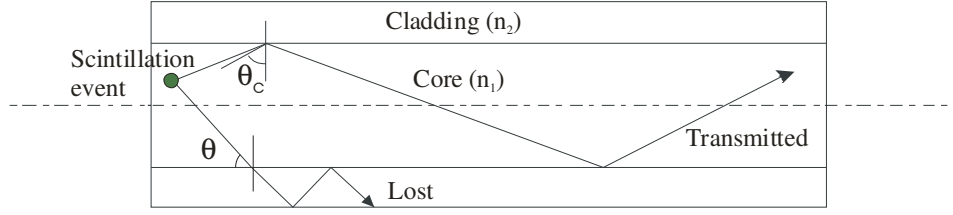
Figure 15. Fiber optic basics.

An incoming light beam that hits a phase boundary against optic thinner medium will be totally reflected within a certain angle. In Figure 15, we see how light beams, generated in the scintillating event, directed to the cladding. When the beam hits the cladding it will be totally reflected if the angle θ is less than, θ_a, according to Snell's law.

$$\theta_c = \sin^{-1}\left(\frac{n_2}{n_1}\right) \tag{9}$$

$$\theta_a = 90° - \theta_c \tag{10}$$

The produced light from the scintillating process is radiated uniformly over 4π steradians. Only the fraction that is directed within the acceptance angel will be transported through the fibre.

The fraction, trapped inside the fibre, in one direction is[28]:

$$\eta = \frac{1}{2}\left[1 + \frac{n_2}{n_1}\right] \tag{11}$$

The scintillating SFOP with LHK-6 glass used in the project have refraction indices of 1,60 for the core (n_1) and 1,48 for the cladding (n_2), Ɛ is only 4%. To improve the efficiency it is common to use a reflective layer at the end surface of the fibres. This will nearly double the efficiency but there are attenuation effects that will decrease transmission efficiency somewhat. This will then produce an η in the range of 6-7%.

The transmission efficiency of a fiber optical image guide is influenced by several factors; numerical aperture (N.A.), bulk absorption, packing efficiency and quality related problems. These quality related problems are caused by manufacturing processes and are defects in core glass, poor interface core/cladding, roundness and geometrical distortions.

$$N.A. = \sqrt{n_1^2 - n_2^2} \tag{12}$$

Two models to predict the transmission efficiency is analyzed. The most common assumption is that all light which is directed to the core/cladding interface with an incident angle higher than the critical angle will be reflected. The meridional[27] analysis assumes that all photons origin from the central axis of the fiber.

The transmission in a fiber calculated by the meridional analysis is:

$$\tau_{\mathrm{m}}(\theta) = T_{n_1,n_0}(\theta)e^{-\frac{\alpha \cdot L}{\cos\theta}} \cdot [1 - \beta(\theta)]^{L \cdot \tan(\theta)/2 \cdot a} \tag{13}$$

15

Where θ is the angle of the light photon in the core. The radius and length is given by a and L. The bulk attenuation coefficient is   . The average loss per reflection at the cladding is β. The number of internal reflections are $L \cdot tan(\theta)/2a$ for a photon with angle θ. The Fresnel transmission factor for the exit out of the fiber into the optical grease is $T_{n1,n0}(\theta)$.

Internal reflection between two transparent optical media, β, results in losses less than 0,001% per reflection[27]. A light beam which is within the acceptance angle would for example be reflected about ten times per mm in a fiber with 50 μm diameter. If the cladding was replaced by a reflective aluminum coating, the losses would be at least 10% per reflection and would be disqualified as light conductor.

The transmission of an arbitrary photon through a fiber has to be handled with skew analysis.
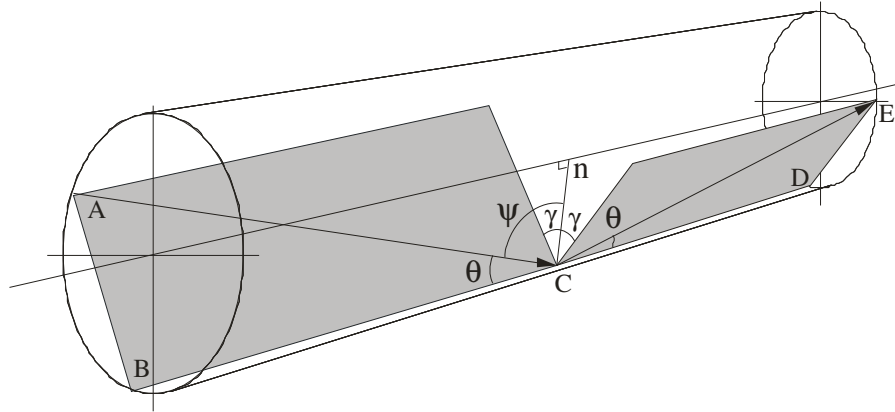
Figure 16. Skew angle analysis.

An incoming photon in the plane ABC is reflected, with an angle Ψ to the normal n, into the plane CDE.

$$\cos(\Psi) \leq \sin(\theta)\cos(\gamma) \tag{14}$$

where θ is the meridional angle and γ is the tilting angle.

$$\gamma = 0 \qquad\qquad \text{for } 0 \leq \theta \leq \theta_a \tag{15}$$

$$\gamma = cos^{-1}[{\sin(\theta_a)}/{\sin(\theta)}] \qquad \text{for } \theta_a < \theta \leq \pi/2 \tag{16}$$

If this model[29] is used, the transmission can be calculated as:

$$\tau_s = T_{n_1,n_0}(\theta)e^{-\frac{\alpha L}{\cos(\theta)}}\int_{\gamma(\theta)}^{\frac{\pi}{2}}[1-\beta(\Psi)]^{\frac{L\tan(\theta)}{2a\cos(\gamma)}}\cos^2(\gamma)\,d\gamma \tag{17}$$

The position, with respect to the distance from the center axis for the attenuated photon, is important. The closer to the periphery of the fiber attenuation, the greater the acceptance angle theta. As the distance from the center axis is close to r/2, the accepted angle is almost 90 degrees. See Figure 17.

It is easy to show that actually photons are attenuated over en area which is circular. That means that a relatively large portion of the photons are attenuated close to the periphery of the circle. If one divides circle as area percent of its diameter, it can be seen that the innermost area with those first 5% of the diameter corresponds to 1 % of the area while the outmost 5% contains 19% of the area.
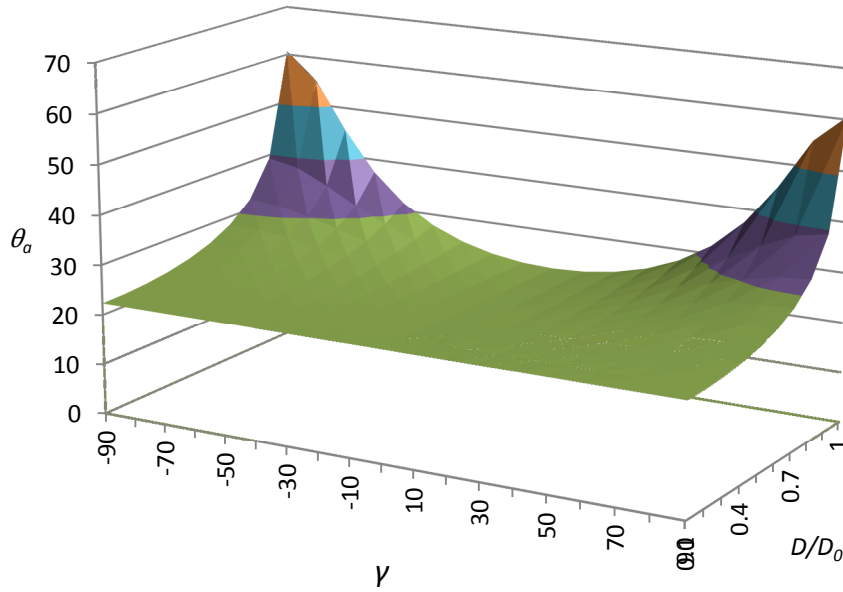
Figure 17. Acceptance angle vs. radial position.

3.5   Lenses

The CCD can be directly coupled to the scintillating screen or relayed with some kind of lens configuration. If the CCD is directly coupled there is no radiation protection from the primary beam. Two options are commonly used, a thick lens equipped with heavy lead glass or moving the CCD out of the primary beam.

Two types of optical lenses will be analyzed in this article, conventional and fiber optical.

A conventional lens is the simplest way to couple the screen to the CCD. The light collection efficiency can be described by[30]:

$$\eta_{lens} = T_{lens}/[2f(1 + m^{-1})]^2 \qquad (18)$$

Where T_{lens} is the transmission through the lens, f is the f-number and m^{-1} is the demagnification. As we want to use a large CCD with high well capacity the demagnification is equal to one ($m^{-1} = 1$). The value for transmission is expected to be about 0.75.

17

The efficiency for an F/1.8-lens is less than 6% and it will have some aberrations that influence the performance. These aberrations are coma, geometrical distortions and vignetting. The lens has also a non-planar surface of best focus which makes correction difficult.

The spatial resolution is degraded especially by the coma. This results in a halo of several hundred μm around each pixel.

A modern aspheric lens minimizes these aberrations but the large number of optical elements required introduces additional flare which decreases the dynamic range. The long range flare itself is limiting the dynamic range to maximum 330 gray scales[30].

3.6   Radiation induced noise

The optically generated signal in an X-ray detector based on indirect detection is only a fraction of the total amount of energy in the attenuated primary X-ray due to conversion losses. As stated earlier the, amount of generated visible photons/X-ray are optimized to be as small as possible but not less than 10 – 20 photons/X-ray. When a 300 keV X-ray is attenuated secondary electrons are created caused by the photo- or the Compton-effect. In the case of silicon (Si), the Compton-effect is dominating due to its low atomic number. The Compton electrons create a large number of electron-hole pairs in the depletion region of the CCD. Studies[31] shows that an average Compton electron from a 300 keV X-ray depose 1.114 keV/μm in a silicon slab with infinite width. In the case of a CCD the energy will be deposit in a pixel with limited width so when secondary electrons are outside the pixel volume it will deposit its energy in the neighbor pixel. Experience from the first generation gave that the radiation induced noise produces white dots with approximately 300 analog to digital units (ADU) above the average level. This corresponds to about 15 keV/X-ray deposited directly in the CCD which is similar as another study[32]. The intention was to design the X-ray camera in such a way that radiation induced noise caused by the primary beam from the X-ray machine will be minimized and thus be negligible. Considering that the camera will be used in radioactive environment where the background radiation is quiet intense, usually in the range from 1 – 10 mSv/h. In such case there will be a large amount of radiation induced noise which is very difficult to avoid. The simulations gave valuable information how thus affecting the CCD and the image quality. It is also important to know the distribution of energy from the radiation induced noise to be able to set a correct threshold when statistical filtering is applied to remove the noise. By dividing an exposure in short sub exposures and comparing the pixel from each sub exposure and reject those values that exceed a threshold value it is possible to minimize the radiation induced noise[5]. As mention earlier the energy is not only deposited in a single pixel. It spills over to the neighbor as well and therefore it is important to exclude the neighbors to the rejected pixels. They are contributing to the noise but usually they are below the threshold and hard to detect in a real X-ray image.

4 Results

The new system has been built and has initially produced very good results. The spatial resolution of the new system is significantly improved compared to the old and this is due to the major improvement of the scintillation SFOP that is the big improvement. Here, we show that modulation of the 13th wire is in the order of 60-70%, which indicates that the modulation of the non-existent 14th wire pair should be better than 20%. It is a hypothetical discussion because there is neither 14:th or 15:th wire pair.

The overall light efficiency in the new system is though a limitation. It will be clear when calculating on detection of 450 kV x-rays through an object of 50 mm steel.

The first step in the detection is created about 8 light detected photons per keV x-ray. The average energy in this case is 300 keV. When attenuation 300 keV photons is 76% Compton-events and 24% photo -effect event. At Compton events on average only half as many secondary electrons created than at photo events where all energy converted. With a transmission efficiency of about 6%, about 90 light photons are leaving the SFOP.

The two image conduits will together have an efficiency of about 15%. Finally, the quantum efficiency of the CCD (which is front-illuminated) is 35%. The overall efficiency of the whole chain is about 5 e⁻ / 300 keV x-ray. The spatial resolution is better but Poisson noise is larger, as can be seen in Figure 18 and in Figure 19.
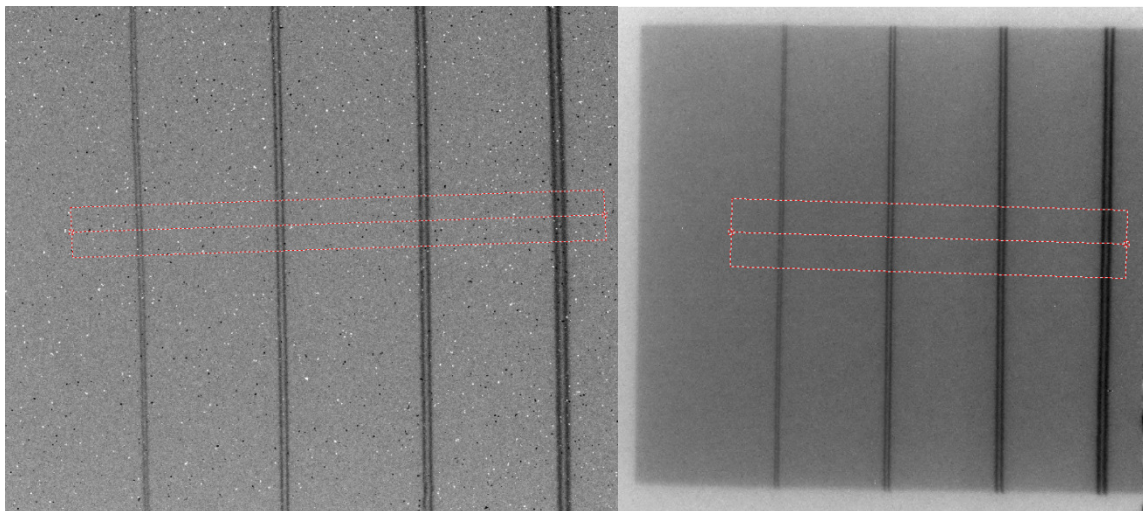
Figure 18. Left: New system, right: Old XIOS-system.
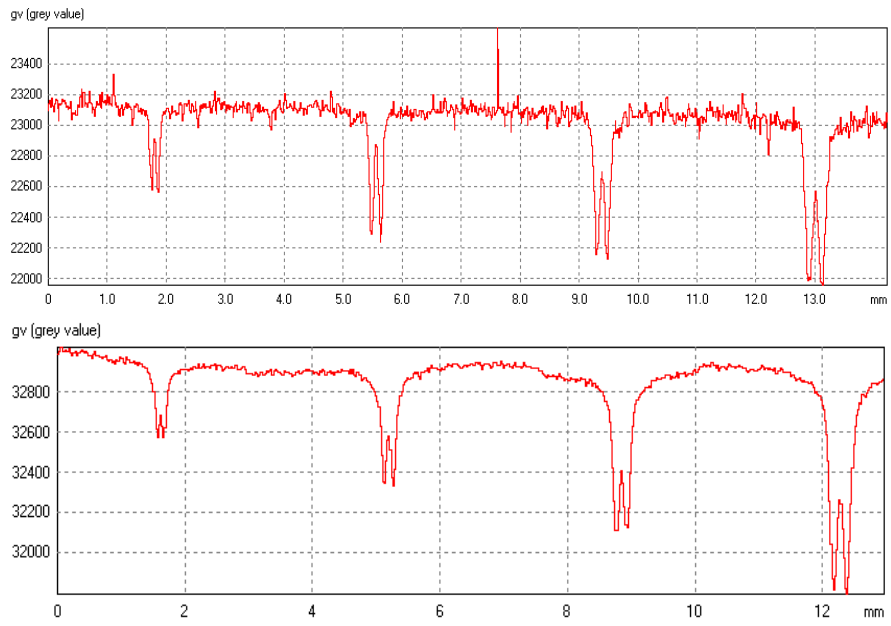
Figure 19. Lineprofils from Figure 18.

5 Summary of appended papers

Paper I: Development of a High Resolution X-ray Radiographic Technique, Optimized for On-site Testing in Radioactive Environments.

A high resolution x-ray radiographic system has been developed, based upon scintillation fiber optics. One of the goals in the design process was to achieve as high overall system resolution as possible. Another was to restrict the size of the components. Hence the system is optimized for sizing and characterization of cracks in nuclear power plants. The system is able to scan the test object from different directions and angles. This paper describes a mathematical model for the two separate, manipulating robots that handles the x-ray tube and the x-ray image detector. It is a general model that is applicable to any arbitrary configurations. A technique to calibrate theirs absolute positions relative to each other has been developed and it is also included a method to use filters, based on statistical methods, to remove noise induced from the radioactive environment.

Paper II: Modelling of High Resolution Radiographic System and Development of a Filtering Technique Based on Wavelet Transformation.

This paper describes a geometrical model of an iron cast object with a number of simple defects included in the volume. This model, together with a model of a specific digital x-ray system and procedure, is used to generate a simulated radiograph of the volume. This is then employed in the development of a filtering technique that extracts the gray-level information related to the existence of anomalies in the object. The wavelet-technique is applied in two different ways in order to identify the large-scale of a matrix (i.e. a radiograph). It turns out that both methods are able to remove the geometrical based information from the grayscale in the simulated radiographs. The techniques are also verified with real radiographs taken from a number of welds and iron cast objects with different kinds of defects and defect sizes. The developed filtering technique is proven to enhance the detection of defects in objects with geometrical variations and has a potential to reduce time-consuming analysis of radiographs. The presented filtering technique is also an important step towards the development of an automated radiographic inspection system.

Paper III: Radiographic Sensitivity Improved by Optimized High Resolution X-ray Detector Design.

A compact imaging detector, based on scintillation fiber optics, has been used for high resolution industrial radiography since 1996. The objective of this paper is to show that the radiographic sensitivity can be improved even further. First, the detection process has been studied by Monte-Carlo simulations and the result shows that the radiation is detected in a very narrow range from the axis of the primary beam. Secondary, Monte-Carlo simulations shows that a bent fiber optic image conduit can eliminate radiation induced noise in the CCD almost completely and reduce the depth of the detector to less than 100 mm.

Paper IV: Novell design of high resolution imaging x-ray detectors.

An x-ray imaging detector, based on scintillating fiber optics, was developed for high energy industrial radiography 1996. It was at that time proven to give superior radiographic sensitivity compared to fine grained industrial x-ray film. This even though the design, at that point, wasn't optimized to protect the CCD from primary radiation. A new imaging detector has now been built based on simulations and experiences from that first generation camera. The objective of this paper is to show how Monte-Carlo simulations were used to optimize spatial resolution and minimize radiation induced noise. Results from various tests of the new detector will be presented which also confirms the simulations at the design stage.

6 Conclusions and future works

Pixel size

It has been shown that with the new scintillating SFOP the spatial resolution has been increased. The pixels size in the CCD used in the project was a bit too small in the new prototype, which should rather have had a pixel size of 20-25 μm. This can be achieved by binning the pixels (2x2) to 27 μm pixels of the new CCD camera. This would increase the light output by a factor from 2.2 to 4.

Image conduit

The prototype used in the project is a commercially available CCD camera with fiber optic input window. As the bent fiber optic lens is coupled through the fiber optic input window, unnecessarily large losses are produced which is a major disadvantage but not unexpected. By re-designing the camera to be used with a single stage bent fiber optic image conduit would increase the light output by a factor of about 2.

Future

Further development of structured scintillation screens, such as curved glass surface and a new concept from Scint-X with channels in Si-matrix filled with CsI(Tl). More validation of the system in a wider range of x-ray energy.

7 References

[1] Jones R.H., Stress-corrosion cracking, p.348, ASM International 1992

[2] Ekström, P., Wåle, J., SKI Report 95:70, p.64-74, Swedish Nuclear Power Inspectorate, 1995

[3] Halmshaw R., Non-destructive Testing, Edward Arnold, 1991

[4] Carlsson, J., Brottmekanik, Hållfasthetslära KTH, p.244, Stockholm 1985

[5] Hammar L., Wirdelius H., 16th World Conference on Nondestructive Testing, Montreal 2004

[6] Shao H., Miller D.W., Pearsall R.C., IEEE Trans. Nucl. Sci., vol. 38, no. 2, pp. 845-857, April 1991

[7] PENELOPE-2008: Code for Monte Carlo Simulation of Electron and Photon Transport, NEA Databank 2009

[8] Shao H., Miller D.W., Nuclear Science Symposium and Medical Imaging Conference, p.341, Nov 1991

[9] Hammar L., 18th World Conference on Nondestructive Testing, Durban 2012

[10] SS-EN 462-5, Non-destructive testing - Image quality of radiographs - Part 5: Image quality indicators (duplex wire type), determination of image unsharpness value.

[11] Dyson N.A., X-rays in atomic and nuclear physics, p.141, Cambridge university press 2005

[12] SS-EN 12543-2, Non-destructive testing - Characteristics of focal spots in industrial X-ray systems for use in non-destructive testing - Part 2: Pinhole camera radiographic method

[13] Knoll, Glenn F., Radiation detection and measurement, p.84, John Wiley & Sons 1999

[14] Harmonex X-ray Calculator, 2369 Laura Lane Mtn. View, CA, USA

[15] ASM Handbook, vol. 17, 9th Edition Metals Handbook, 1989

[16] XCOM Database, The National Institute of Standards and Technology (NIST)

[17] Attix F.H., Introduction to radiological physics and radiation dosimetry, p.124, John Wiley & Sons

[18] Particle acceleration and detection, Inorganic Scintillators for Detector Systems, p.84, Springer 2006

[19] Shinzou Kubota, Journal of the Physical Society of Japan, Vol. 69, No. 10, October, 2000, pp. 3435-3440

[20] Particle acceleration and detection, Inorganic Scintillators for Detector Systems, p.58, Springer 2006

[21] Shao H., Miller D.W., Pearsall R.C., Nucl. Instr. and Meth. A299 (1990) p.528

[22] Badano A., Med. Phys. 31 (11), p.3122, November 2004

[23] Zanella G., Nucl. Instr. And Methods, A 382, p.567, 1996

[24] Yaffe M.J., Rowlands J.A., Phys. Med. Biol. 42, p.1, 1997

[25] Hammar L., Wirdelius H., Int. Symposium on Digital Industrial Radiology and Computed Tomography, Lyon, 2007

[26] X-ray Data Booklet, Lawrence Berkeley National Laboratory, 2009

[27] Maidment Andrew D.A., Phys. Med. Biol. 41, p.475, 1996

[28] White T.O., Nucl. Instr. And Methods, A 273, p.820, 1988

[29] Potter R.J., J. Opt. Soc. Am. 51, p.1079, 1961

[30] M.W. Tate, D. Chamberlin, S.M. Gruner, Review of Scientific Instruments 76, 2005

[31] Burke E.A., Boyle J.J., Huemmler H.J., IEEE Trans. Nuclear Science, Vol. 28, No. 6, 1981

[32] Jenkins W.C., Killiany J.M., Saks N.S., IEEE Trans. Nuclear Science, Vol. 28, No. 6, 1981